Pyrolysis of a metal-organic framework followed by *in situ* X-ray absorption spectroscopy, powder diffraction and pair distribution function analysis

Mads Folkjær,[a,b] Lars F. Lundegaard,[c] Henrik S. Jeppesen,[a] Melissa J. Marks,[a] Mathias S. Hvid,[a] Sara Frank,[b] Giannantonio Cibin,[d] and Nina Lock[e]*

[a]Interdisciplinary Nanoscience Center (iNANO), Aarhus University, Gustav Wieds Vej 14, DK-8000 Aarhus C, Denmark

[b]Department of Biological and Chemical Engineering, Aarhus University, Åbogade 40, DK-8200 Aarhus N, Denmark

[c]Haldor Topsøe A/S, Haldor Topsøes Allé 1, DK-2800 Kgs. Lyngby, Denmark

[d]Diamond Light Source Ltd., Harwell Science and Innovation Campus, Didcot, OX11 0DE, UK

[e]Carbon Dioxide Activation Center (CADIAC), Department of Biological and Chemical Engineering and iNANO, Aarhus University, Åbogade 40, DK-8200 Aarhus N, Denmark

*Corresponding author: nlock@bce.au.dk

Abstract

Metal-organic frameworks (MOFs) can serve as precursors for new nanomaterials *via* thermal decomposition. Such MOF-derived nanomaterials (MDNs) are often comprised of metal and/or metal oxide particles embedded on porous carbon. The morphology of MDNs is similar to that of the precursor MOF, and improved stability and catalytic properties have been demonstrated. However, the pathway from MOF to MDN is only well understood for a few systems, and *in situ* studies are needed to elucidate the full phase behaviour and time/temperature dependency. In this work, we follow the MOF-to-MDN transformation *in situ* by using three complementary techniques: X-ray absorption spectroscopy (XAS), powder X-ray diffraction (PXRD), and X-ray total scattering/pair distribution function (TS/PDF) analysis. The thermal decomposition of HKUST-1, i.e. the archetypical MOF Cu_3(btc=1,3,5-benzenetricarboxylate)$_2$, is followed from room temperature to 500 °C by applying different heating ramps. Real space correlations are

followed by PDF and Extended X-ray Absorption Fine Structure (EXAFS), and quantitative phase fractions are obtained by refinement of PXRD and PDF data, and by linear combination analysis (LCA) of X-ray Absorption Near-Edge Structure (XANES) data. We find that HKUST-1 decomposes at 300-325 °C into copper(I) oxide and metallic copper. Above 350-470 °C, metal particles remain as the only copper species. There is an overall good agreement between all three techniques with respect to the phase evolution, and the study paves the road towards rational synthesis of a Cu_2O/Cu/carbon material with the desired metal/metal oxide composition. More importantly, our investigations serve as a benchmark study demonstrating that this methodology is generally applicable for studying the thermal decomposition of MOFs.

1 Introduction

Metal-organic frameworks (MOFs) are a class of porous materials consisting of metal nodes connected *via* rigid organic linker molecules. The term was coined in 1994,[1] and the possibilities of reticular chemistry seem almost endless with more than 88,000 reported MOF structures.[2] They have emerged as promising candidates for various applications including gas separation, gas storage, and sensing properties.[3-6] Moreover, MOFs are especially attractive within catalysis as their composition allows for advanced engineering of active sites.[4] While major steps have been taken to improve the stability of MOFs,[7] some intrinsic issues still plague most, such as lower thermal and chemical stabilities in comparison with their inorganic counterparts such as metal oxides.[8-12] The lacking stability is associated with e.g. the breakage of metal-linker bonds or of the linkers themselves, pore collapse, water degradation, limited pH tolerance, or solvent assisted linker exchange in electrolytes. Such stability issues may result in framework degradation under working conditions.

In recent years, MOFs have shown to serve as precursors for new interesting nanomaterials.[13-16] A very common method to accomplish such compounds is to heat the MOF to decomposition under inert gas flow (defined as pyrolysis). This often results in metal and/or metal oxide nanoparticles embedded in a porous carbonaceous matrix with greatly improved stability and electrical conductivity compared to their parent structure. Size, shape, porosity, and other descriptors of the daughter MDN are inherently connected to the parent MOF, meaning that this synthesis methodology unlocks a new type of rational design of complex nanomaterials. MDNs have shown to be useful within similar applications as described for MOFs, and particularly works on electrocatalysis seems encouraging.[13, 17]

Although the MDN field is growing at a fast rate, the mechanism behind the transformation from parent MOF to daughter MDN is not yet understood in great detail. The structure of the pyrolyzed material depends on the specific conditions of the thermal treatment (e.g. the temperature profile and gas flow).[18-22] Moreover, the structural transition is likely to occur gradually during the pyrolysis, and a product heated at a high temperature for short time may result in a kinetic product, while heating for longer time may result in a thermodynamic product. Only one of the products may be desired for its specific applications. For example, it may be beneficial to interrupt the pyrolysis at an intermediate stage to obtain nanoparticles with a given size or phase composition. In order to understand the pyrolysis of MOFs in-depth and to explore the possibility of preparing materials with a given composition, fundamental knowledge on the structural evolution with temperature and time should be investigated by *in situ* structural studies. Studies using *in situ* structural probes for the investigation of MOF decomposition are still few (STEM-EDX,[23] PXRD,[24, 25] XAS,[26, 27] FTIR,[25] DRIFTS,[27, 28], and Mössbauer spectroscopy[27]). However, detailed *ex situ* studies exist, including a recent study combining pair distribution function (PDF), X-ray absorption spectroscopy (XAS), and X-ray diffraction.[29]

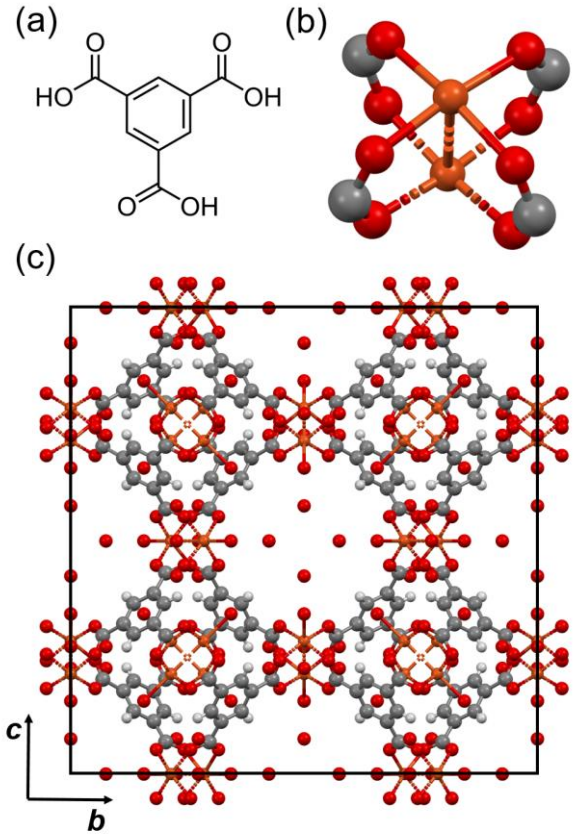

Fig. 1. HKUST-1 consists of a) the organic linker 1,3,5-benzenetricarboxylate (btc), here shown as H_3btc and b) the so-called copper(II) paddlewheel, i.e. [$Cu_2(COO)_4$], as the secondary building unit. c) HKUST-1 is microporous with pore sizes of approx. 1 nm and has a cubic crystal structure (a = 26.343 Å, CCDC 112954[30]). The unit cell is shown in black, copper is shown in orange, oxygen in red, and carbon in grey. Hydrogen atoms have been omitted for clarity.

In this work, we investigate the pyrolytic transformation of the archetypical MOF Cu_3(btc=1,3,5-benzenetricarboxylate)$_2$ which is also known as HKUST-1 (Fig. 1). HKUST-1 is comprised of so-called paddlewheel copper(II) secondary building units, i.e. [$Cu_2(COO)_4$], in which the carboxylates from four different btc linkers coordinate to two Cu(II) atoms. This results in a three-dimensional cubic framework with approx. 1 nm pores.[30] If the compound is exposed to moisture, one water molecule coordinates to each Cu(II), and additional water may be present in the pores. The structure is originally reported to be stable to temperatures around 240 °C, but the solvothermal synthesis procedure used in this work has shown thermal stability

of HKUST-1 to approx. 350 °C under inert conditions.[31] When heating HKUST-1, before thermal decomposition, solvent water molecules in the pores and ligand water molecules evaporate to give under-coordinated copper(II) sites.

Several examples of using HKUST-1 as precursor for MDNs exist, and HKUST-1-derived materials have shown promise for various applications such as sensoring,[32-34] batteries,[35-38] and catalysis (e.g. CO oxidation,[39-41] electrocatalytic CO_2 reduction,[42-45] and more[46-51]). There is consensus that the pyrolysis product formed inherits the octahedral morphology of the parent MOF crystals. The pyrolyzed samples, particles of copper and/or copper oxides are anchored on the surface of a porous carbon matrix with octahedral-like morphology. There is also a general agreement that under inert conditions copper metal is always formed, but different studies have also found copper(I)- and/or copper(II) oxide.[39, 42, 48, 52] This underlines the fact that fundamental understanding of the pyrolysis is needed to control the synthesis of MDNs.

Herein, we present a benchmark *in situ* study investigating the phase evolution of HKUST-1 during pyrolysis by combining the three structural probes: synchrotron based X-ray absorption spectroscopy (XAS), X-ray total scattering and pair distribution function (PDF) analysis, and in-house powder X-ray diffraction (PXRD). PDF analysis and XAS are important techniques in solving structures of crystallographically challenged materials (e.g. amorphous, nanosized, or defect-rich) since these methods probe the local structure without crystallinity as a prerequisite. PXRD, in contrast, is ideal for studying materials with long-range order. In this study, the phase evolution of the different copper species was determined by applying a temperature profile from room temperature (RT) to 500 °C.

We explored the degradation of a crystalline MOF to also investigate the consistency between the three techniques, and good agreement between PXRD, PDF and XAS is observed. Thereby,

the study verifies that the methodology can be generally applied to follow the thermal decomposition of MOFs. By combining the three techniques, complementary information is obtained with respect to crystalline and amorphous phases. However, one or two methods alone may uncover the mechanism behind the thermal degradation depending on whether the MOF, MDN and intermediates are crystalline or amorphous.

2 Experimental section

All chemicals were purchased from Sigma-Aldrich and used without any further purification.

2.1 Synthesis of HKUST-1

HKUST-1 was prepared according to a previously reported procedure.[29] $Cu(NO_3)_2 \cdot 2.5H_2O$ (3.35 g, 14.4 mmol) was dissolved in 48 mL deionized water. 1,3,5-benzenetricarboxylic acid (1.68 g, 8.0 mmol) was dissolved in 48 mL ethanol. The two solutions were mixed, stirred, and transferred to 23 mL Teflon lined stainless steel autoclaves (approx. 9.6 mL in each autoclave). The sealed autoclaves were heated in a convection oven to 120 °C for 12 hours. The reaction mixtures from the autoclaves were filtered and washed with deionized water and ethanol, and the cyan coloured powder was left to dry in air.

2.2 *Ex situ* characterization of HKUST-1

Scanning electron microscopy (SEM): The size and morphology of pristine and pyrolyzed HKUST-1 (i.e. the powder obtained after an *in situ* total scattering experiment using a heating ramp of 2 °C/min) were investigated by scanning electron microscopy on a FEI-Nova Nano-SEM 600 under high vacuum conditions. The powder samples were mounted on adhesive car-

bon tape, and a 6.0 nm Pt layer was subsequently deposited using a LEICA EM SCD 500 vacuum film-deposition system equipped with a LEICA EM QSG100 Quartz Crystal Film Thickness Monitor.

Elemental analysis: Elemental CHNS analysis was performed on pyrolyzed HKUST-1 powder on an Elementar Vario MACRO Cube instrument. Prior to analysis approximately 20 mg of sample was mixed with WO_3 powder as catalyst. Three replicas were analysed.

2.3 *In situ* X-ray Absorption Spectroscopy

In situ XAS was performed on the Cu *K*-edge in transmission mode at the B18 beamline at the Diamond Light Source in Oxford, UK.[53] A capillary furnace setup provided by the beamline was used (Fig. S3). Powder of HKUST-1 was diluted by boron nitride and pressed to a pellet. To obtain a suitable absorption edge step, the optimal sample amounts of boron nitride and HKUST-1 was estimated using the software XAFSmass.[54] A chip of the pellet was inserted into a 3 mm quartz capillary, which was connected to the beamline mass flow controllers using Swagelok tubing, and the sample was purged by a nitrogen flow of 100 mL/min. The sample was heated from RT to 500 °C by indirect resistance heating with a heating ramp of 3 °C/min. Transmission spectra covering both the X-ray absorption near-edge structure (XANES) and extended X-ray absorption fine structure (EXAFS) region (200 eV below the edge to 850 eV above the edge) were collected in continuous scan mode with an acquisition time of approx. 90 seconds per spectrum. The X-ray energy was selected using a double crystal Si(111) monochromator, and spectra on a copper metal foil were measured simultaneously for energy calibration.

Data treatment was carried out in Athena from the Demeter software package.[55] The EXAFS ($\chi(k)$) was obtained with a spline range of k=0.5-13 Å^{-1}, and a k^2 weighting. The EXAFS Fourier

transforms ($\chi(R)$) were obtained by using data in the k-range of 1.5-12 Å^{-1}, a k^2 weighting, and a Hanning window.

Spectra were measured *ex situ* for standard samples of copper(I) oxide, copper(II) oxide, and copper(II) acetate. Powders were diluted with cellulose and pressed into pellets, and data were collected in transmission mode. A spectrum of copper metal was obtained from the copper foil used for energy calibration. To obtain the $\chi(k)$ and $\chi(R)$ for these samples, a spline range of 0.5-16 Å^{-1} and a k-range of 1.5-14 Å^{-1}, respectively, were used.

Linear combination analysis (LCA) fitting of XANES spectra was carried out in Athena over the energy range -15 to +40 eV in regard to E_0. All phase contents were restrained to values between 0 and 1, and the sum of the phase contents to 1. The phase contents were converted from percentage of copper atoms to weight percentage of the different constituents.

2.4 *In situ* Powder X-ray Diffraction

In situ PXRD was performed on a PanAlytical Empyrean instrument in reflection mode with Bragg–Brentano geometry and a Cu $K\alpha$ source (λ = 1.541 Å). As a part of the sample preparation, the largest particles were removed gravimetrically from the powder to avoid textured scattering. A 2 °C/min heating ramp was applied in steps of 25 °C (from 25 °C to 500 °C), and data sets were collected while keeping the temperature constant. Three data sets were collected (10 min each in the range 5-75° 2θ) per step, resulting in an average heating rate of 0.72 °C/min (see Fig. S2). The experiment was performed in an inert nitrogen gas flow of 100 mL/min. PXRD data were refined using the Rietveld method as implemented in the TOPAS software,[56] and for the definition of the instrument profile function the fundamental parameters approach was used.[57] One size parameter[58] was refined for each of the three crystalline phases, *i.e.* HKUST-1, Cu_2O and Cu (see details in the ESI). Calculated diffractograms were obtained using the Mercury software[59] from the crystal structures of HKUST-1 (i.e. hydrated CCDC 11295412

and dehydrated CCDC 105054131), Cu (ICSD 5225632), Cu_2O (ICSD 5204333), and α-alumina (ICSD 25778). The same crystal structures were used as starting models for the Rietveld refinements.

2.5 *In situ* X-ray Total Scattering and Pair Distribution Function Analysis

The *in situ* total scattering experiments were performed at the P02.1[60] (λ=0.2073 Å) and P21.1 (λ=0.1204 Å) beamlines at PETRAIII of the Deutsches Elektronen-Synchrotron (DESY) in Hamburg, Germany. We used a custom-built capillary setup which has previously been described in detail by others (Fig. S17).[61] HKUST-1 powder was packed in fused silica capillaries (inner diameter 0.7 mm, outer diameter 0.85 mm) allowing a high transmission of X-rays. The capillary was connected to the reactor using graphite ferrules and Swagelok fittings enabling a gentle argon flow of 100 mL/min through the capillary. The sample containing capillary was heated by a jet of hot air from directly below. Experiments using different heating ramps from RT to 500 °C were performed: 2 °C/min at P21.1, and 5 °C/min, and rapid heating (i.e. reaching the target temperature within 8-10 s) at P02.1. The heating profile for each experiment is sketched in Fig. S2, and it is noticeable that heating at 2 °C/min was continuous, while heating at 5 °C/min was performed stepwise. Due to time constraints, the 2 °C/min PDF consisted of an initial 25 °C/min ramp until 325 °C was reached, after which the desired 2 °C/min heating ramp was employed. The actual temperature inside the capillary might vary slightly between the different experiments, as in these experiments, it was not possible to monitor the temperature inside the capillary during the pyrolysis experiment. Instead, a thermocouple was inserted into the capillary before the experiments for temperature calibration.

At both beamlines, *in situ* total scattering data were acquired on an amorphous silicon two-dimensional (2D) flat panel Perkin Elmer XRD1621 detector (40x40 cm^2, pixel size of

200x200 um^2) in full ring configuration with an angular resolution of Q_{max}=25.5 Å^{-1} and 19.7 Å^{-1}, respectively, at P21.1 and P02.1.

The software Dioptas[62] was used for azimuthal integration of the 2D total scattering data images. PDFgetX3[63] and the user interface xPDFsuite[64] were used for subtraction of the integrated intensities of an empty capillary and to obtain the $S(Q)$, $F(Q)$, and $G(r)$ functions. A Q-range of 0.6-22.3 Å^{-1} was used for the Fourier transformation of P21.1 data, while data in the range 0.5-19.7 Å^{-1} and 0.5-15.2 Å^{-1}, respectively, were used for the 5 °C/min and rapid heating data from P02.1. In both cases an R_{poly}=1.1 was applied. Data were collected on CeO_2 (P21.1) and LaB_6 (P02.1) standards to calibrate the distance from sample to detector, in addition to the instrumental Q_{broad} (0.008675 at P21.1, 0.007331 at P02.1) and Q_{damp} (0.04060 at P21.1, 0.04500 at P02.1) parameters. Multiphase real-space refinements were performed on the obtained PDF functions ($G(r)$) in PDFgui[65] in r-ranges of 1-15 Å and 1-40 Å. Refined was the scale factor of HKUST-1, Cu_2O and Cu, the cubic unit cell parameters of the three phases, and two isotropic atomic displacement parameter, i.e. one to describe all copper atoms and one to describe all carbon and oxygen atoms. Moreover, the delta2 parameter was refined. Theoretical PDFs of the different crystal structures were calculated in PDFGui based on CIF data (HKUST-1 hydrated CCDC 11295412, HKUST-1 dehydrated CCDC 105054131, Cu ICSD 5225632, and Cu_2O ICSD 5204333). The same crystal structures were used as starting models for the data refinements described above.

3 Results and discussion

3.1 *In situ* X-ray absorption spectroscopy

Information on the evolution of the oxidation state and local geometry of the copper atoms at increasing temperature can be extracted from the XANES region of the *in situ* XAS measure-

ments (Fig. 2). This was done by comparing the time-resolved data with data collected on copper standards. By heating the sample from room temperature to 300 °C, the XANES features do not change, i.e. the [$Cu_2(COO)_4$] paddle-wheel motif containing copper(II) remains. In the temperature range 300-360 °C (equivalent of 20 minutes heating), the reduction of copper is seen by a shift of the edge position towards lower photon energies. The spectral features significantly change: Below 300 °C, i.e. corresponding to HKUST-1, a distinct peak feature is seen at 8986 eV (A2 in Fig. 2) with small broad shoulder features at 8981 eV (A1) and 8993 eV (A3), and a white line-like maximum at 8999 eV (A4). Furthermore, the EXAFS oscillations give rise to a broad dip in the signal around 9025 eV. The XANES spectra up to 300 °C show a large similarity with copper(II) acetate, which also contains [$Cu_2(COO)_4$] paddle-wheels, hence a similar local geometry around copper(II). We suggest the small feature at 8981 eV (A1) in the spectra of HKUST-1 arises from an impurity of copper(I) oxide in the as-synthesized HKUST-1. This is further verified in the PXRD and PDF analysis (see later sections); we were unaware of this impurity when the experiments were performed.

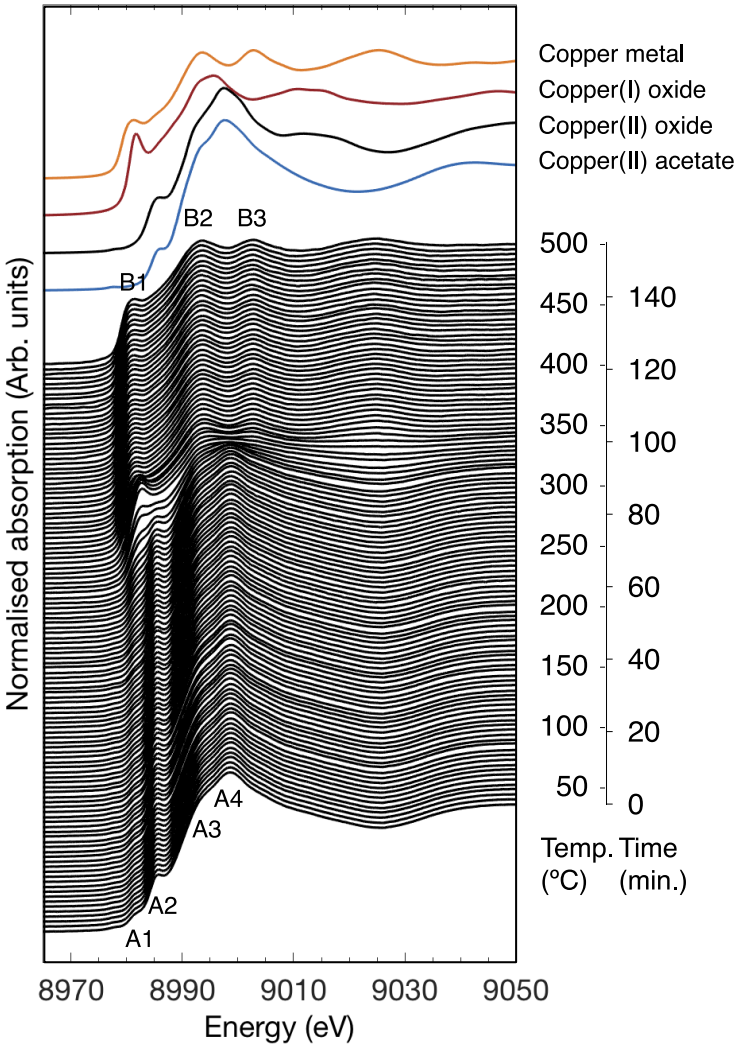

Fig. 2. *In situ* XANES spectra of HKUST-1 during pyrolysis at 3 °C/min. Four relevant standards are shown in top of the plot: copper metal (yellow), copper(I) oxide (red), copper(II) oxide (black), and copper(II) acetate (blue). Labels A1-A4 and B1-B3 function as guides to the eye to highlight features in the spectra. A combined temperature/time axis is shown.

Above 300 °C, A2-A4 disappear as A1 characteristic of copper(I) oxide becomes sharper and more intense, before it eventually disappears around 350 °C. An edge shoulder at 8982 eV (B1) from metallic copper is identified together with two features just above the edge jump at 8994 eV (B2), and 9003 eV (B3), which remain upon further heating. A local maximum in the EXAFS data at 9025 eV is furthermore seen, which is consistent with metallic copper. Above

360 °C, the spectra only contain features from metallic copper. Thus, from a qualitative XANES fingerprint analysis, the pyrolytic transformation to HKUST-1 proceeds to metallic copper *via* copper(I) oxide.

The composition of the sample of interest can be quantified by linear combination analysis (LCA) if the phases contained are properly described by standard copper samples. The first spectrum of the *in situ* series was used as the HKUST-1 standard, meaning the small amount of copper(I) impurity is 'hidden' in this analysis. The LCA performed on the *in situ* XANES data series leads to a phase content evolution (Fig. 3 and Table S2) in agreement with the qualitative analysis above (see examples of fits in Fig. S4). Below 300 °C the spectra can primarily be described as HKUST-1. The fit obtained based on data collected at approx. 330 °C, i.e. with large amounts of copper(I) oxide, is relatively poor, and the weight fraction value cannot be trusted completely. While the edge position, hence the oxidation state, of spectra in this temperature range is described reasonably well, the features characteristic of the coordination around copper are not well described. This probably arises from the fact that the bulk crystalline standards do not properly describe the decomposing MOF and/or the nanostructured (and potentially amorphous) copper metal and oxide.[66-68] The presence of an amorphous content is in agreement with PXRD and PDF data (see later sections) and explains the moderate quality of the LCA fit of these data. Above 356 °C, no appreciable changes occur with metallic copper being the only product.

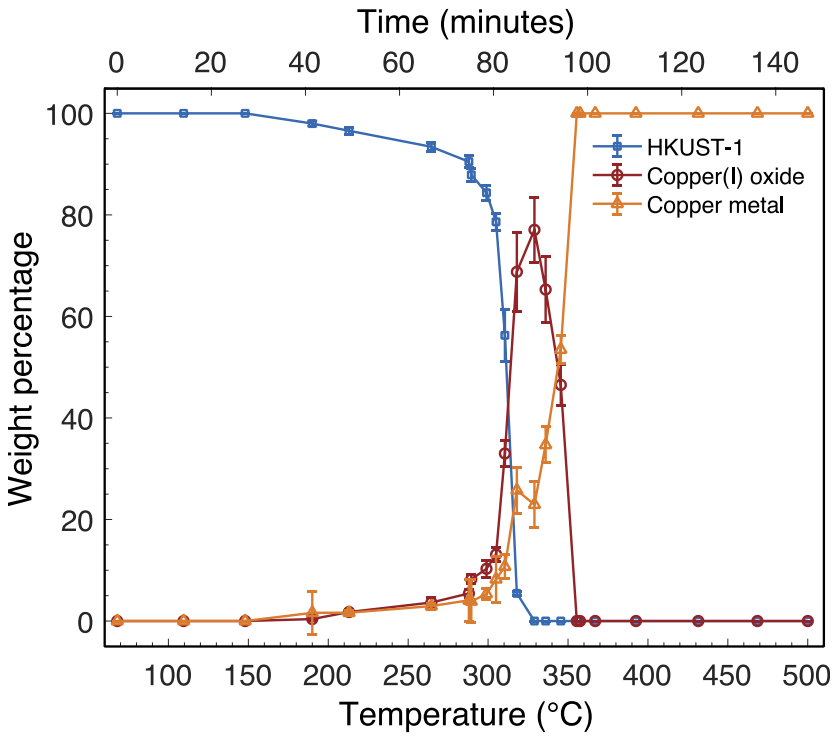

Fig. 3. Phase content evolution (in weight percent) during HKUST-1 pyrolysis (3 °C/min) as extracted from LCA fitting of XANES data. Three standard spectra were fitted to the data: HKUST-1 (blue), copper(I) oxide (red), and copper metal (yellow). The HKUST-1 'standard' is hydrated and from the same batch as the powder used in the heating experiment, which explains why the impurity of copper(I) oxide is not found from this analysis. Hence, here a HKUST-1 content of 100 % corresponds to as-synthesized HKUST-1 containing an impurity of Cu_2O (estimated by PDF analysis to be 9.0 wt%).

The EXAFS region provides complementary information on the local structure around copper. Characteristic interatomic distances involving copper are obtained by the Fourier transform of the EXAFS (Fig. 4, see EXAFS spectra in Fig. S5). Up to approx. 320 °C, the correlations are unchanged with the 1.5 Å peak assigned to Cu-O from the carboxylate group in the btc linker. The peak at 2.2 Å is from Cu-Cu in the paddle-wheel motif. In the range 330-350 °C, the Cu-O peak decreases in magnitude, while a peak at 2.2 Å describing the Cu-Cu nearest neighbour distance in metallic copper emerges and eventually becomes the only correlation present. This further proves that metallic copper is the final product. Around 330 °C, the Cu-O peak seems

to shift slightly by approx. 0.1 Å to lower *R* before vanishing, which is consistent with Cu-O in copper(I) oxide.

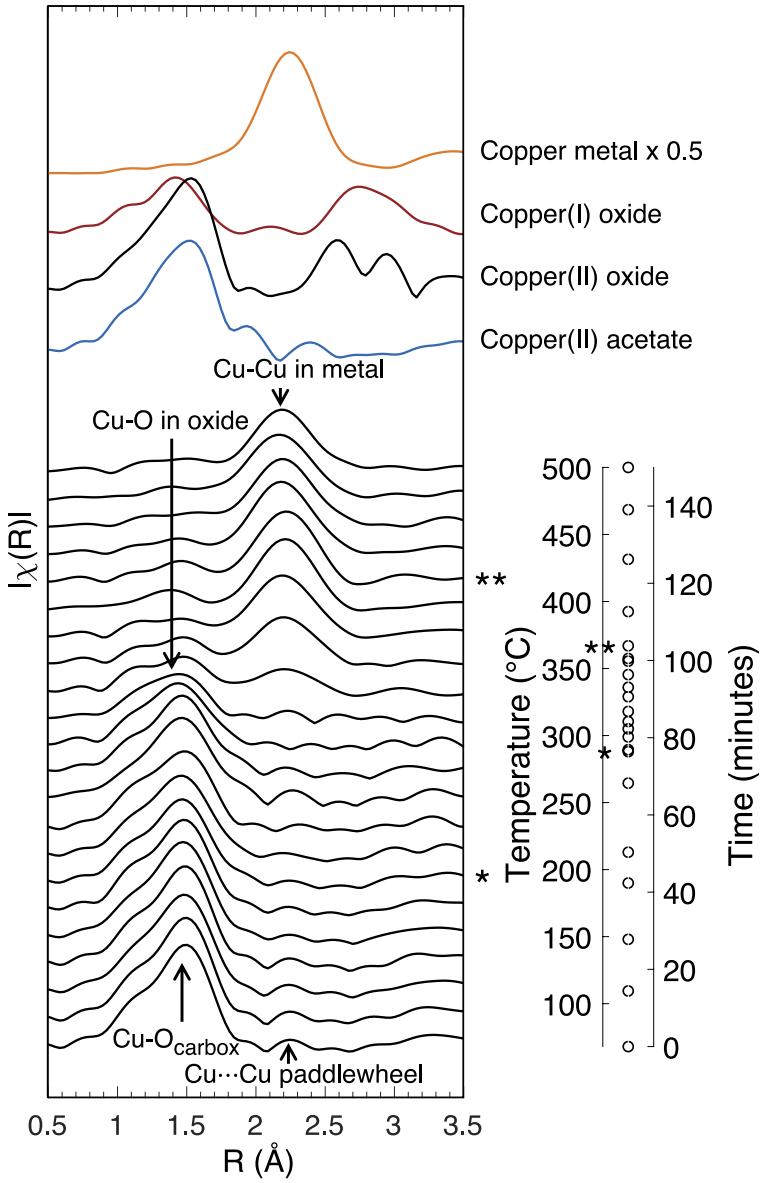

Fig. 4. The Fourier transform magnitudes in *R*-space (not phase corrected) of the *in situ* EXAFS data collected during HKUST-1 pyrolysis. Four relevant standards are shown in top of the plot: Copper metal (yellow, scaled by 50%), copper(I) oxide (red), copper(II) oxide (black), copper(II) acetate (blue). Arrows indicate the most important correlations involving copper. A combined temperature/time axis is shown in the right of the figure. As the Fourier transforms do not represent EXAFS spectra equidistant in temperature/time, asterisks (* and **) are used to indicate the start and end of a narrower temperature interval where most of the chemistry occurs, i.e. 288-367 °C. Open circles (o) indicate temperatures at which data are shown.

3.2 *In situ powder* X-ray diffraction and Rietveld analysis

The long-range structural order of HKUST-1, the crystalline intermediates and products of the pyrolysis were investigated using *in situ* PXRD with an in-house instrument. Below 300 °C, Bragg reflections from HKUST-1 are identified, and from close inspection of the data, weak broad peaks from impurity copper(I) oxide are identified (Fig. 5). At 300 °C, upon thermal decomposition of the framework, the diffractogram exhibits a low signal-to-noise ratio (Fig. S9). Peaks from HKUST-1 are still visible, the oxide signal grows in intensity (see the broad peak from the (111) reflection in Fig. 5), and peaks from metallic copper are observed (e.g. at 43.0° and 50.1° 2θ). At higher temperatures, HKUST-1 has fully decomposed, and no signal is observed for the MOF, while the oxide remains until 348 °C, after which intense sharp peaks from the metal contribute solely to the diffractograms (Fig. 5 and S6-S15). Peaks from α-alumina is observed after the decomposition of the MOF, due to cracks in the sample exposing the underlying alumina sample holder. The α-alumina sample holder peaks are clearly observed in the 50-70° 2θ range.

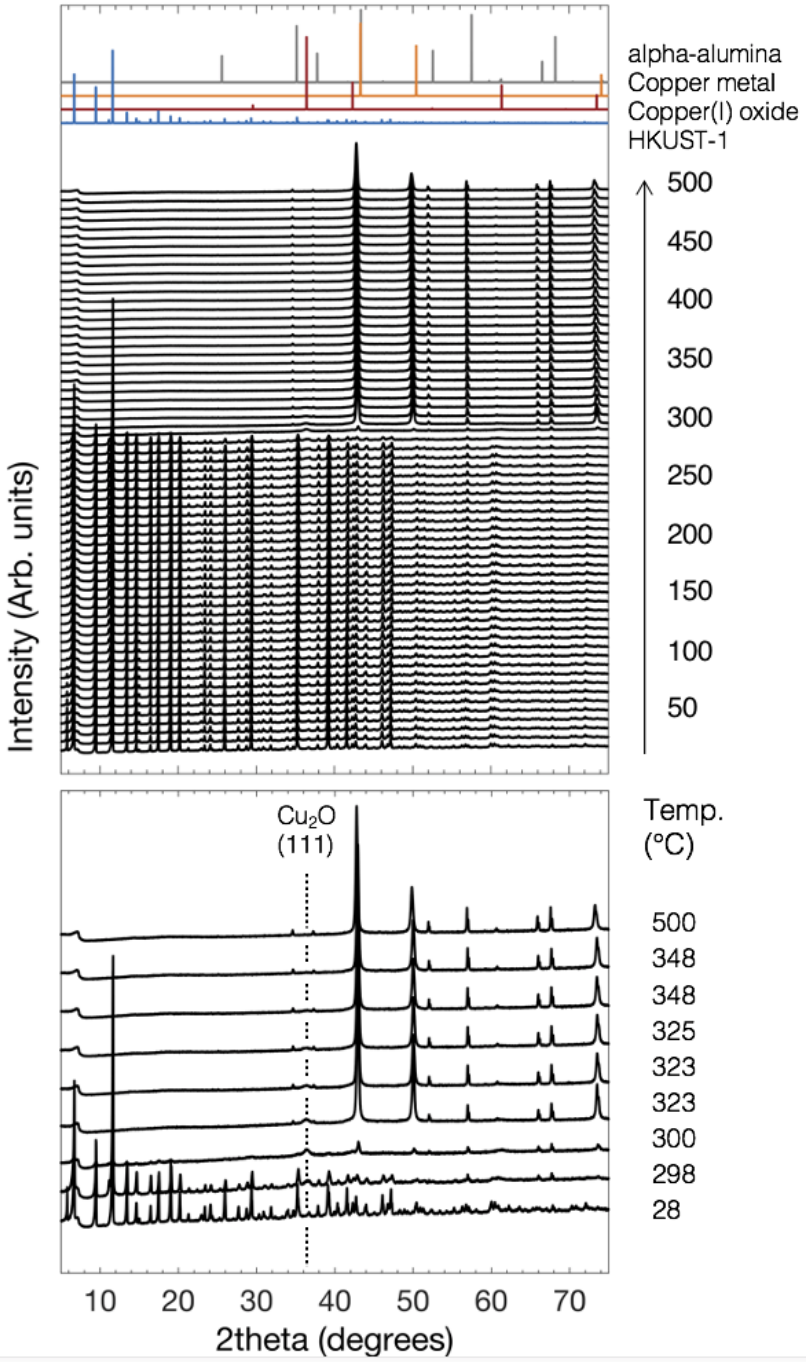

Fig. 5. *In situ* PXRD of HKUST-1 pyrolysis with calculated diffractograms of α-alumina (grey), copper metal (yellow), copper(I) oxide (red), and HKUST-1 (blue). The bottom figure shows the diffractograms around the decomposition point (and the first and last pattern as reference) where the broad (111) peak from copper(I) oxide is highlighted. The α-alumina peaks are due to the exposed sample holder after decomposition.

The evolution of the phase contents, and structural information including the unit cell parameters and crystallite sizes were obtained from sequential Rietveld refinements. The refinements

are in general good with low R_{wp} values and small difference curves (Fig. S6-S15 and Table S3). The phase contents as a function of the temperature show that the MOF is stable to approx. 300 °C (Fig. 5 and 6). Above this, first the scale factor of HKUST-1 drastically decreases, immediately followed by the formation of copper(I) oxide and metallic copper from the reduction of HKUST-1.

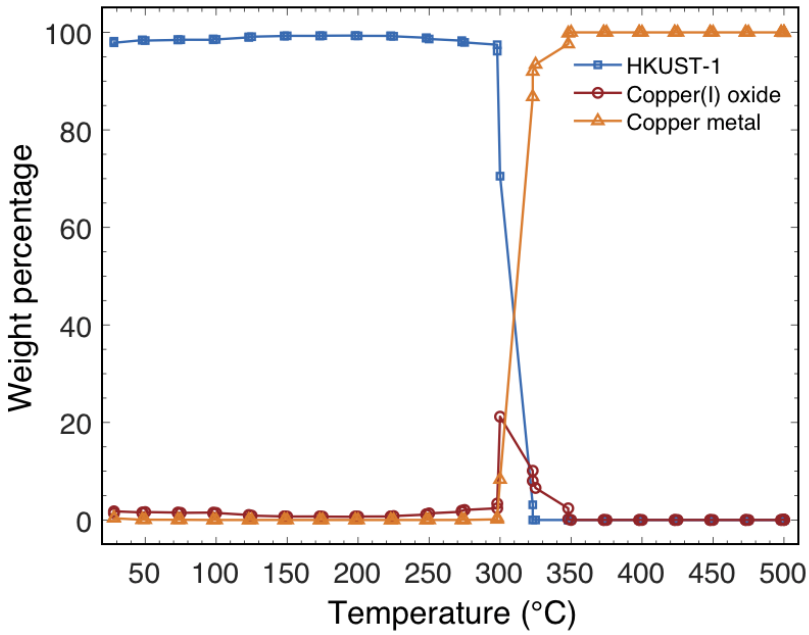

Fig. 6. Phase content evolution of HKUST-1 pyrolysis as obtained from Rietveld refinement of PXRD data: HKUST-1 (blue), copper(I) oxide (red), and copper metal (yellow).

The crystalline copper(I) oxide impurity in the as-synthesized sample of HKUST-1 was quantified to 1.6 wt%. By refining the oxygen occupancies of pore water and the water ligands, it is found that above 73 °C, the pore solvent has fully evaporated from HKUST-1, while the chemically bound water is fully removed around 200 °C. The copper(I) oxide constitutes 21.2 wt% of the mixture at its maximum at 300 °C. Upon further heating, copper(I) oxide is reduced to metallic copper which is the final constituent above approx. 350 °C. The oxide and metal, respectively, exhibit nanosized dimensions of approx. 10-13 nm and 65-80 nm (Fig. S16). It is worth noticing that the metallic nanoparticles do not grow in size during heating at 350-500 °C,

which we suggest might be due to an anchoring or confinement of the copper particles at the carbon matrix. In comparison, SEM images reveal octahedral particles of 10-30 μm with either submicron perforations or a covering of 300-400 nm faceted copper particles (Fig. S1).

It is worth noting, that the diffractogram measured at 300 °C where the MOF decomposition takes place is collected over 10 minutes, which means that in the time the angular range is scanned, the sample mixture changes, i.e. the low angle and high angle part of the diffractogram might not reflect the same sample. However, a reasonable fit is still achieved with the note that the refined composition and structural parameters have an increased uncertainty compared to the remaining data.

3.3 *In situ* X-ray total scattering and pair distribution function analysis

Pair distribution function (PDF) analysis reveals both the local and medium range order in the bulk sample, and is complementary to the element specific XAS methods probing only the local environment around copper. Total scattering data were collected at a heating ramp of 2 °C/min, and data represented as the reduced total scattering function $F(Q)$ is displayed in Fig. S18. The corresponding PDF data in the range r = 1-10 Å is shown in Fig. 7, while PDF data in the range 1-50 Å is displayed in Fig. S19. At temperatures below approx. 325 °C, the only changes in the peak-peak correlations arise from solvent evaporation as seen above 100 °C by the loss of a peak at 2.3 Å from Cu-O_{aqua} and an emerging peak at 2.5 Å, which is assigned to the paddle-wheel Cu-Cu correlation (Fig. 7). Before removal of the water ligand, this Cu-Cu correlation was longer and part of the overlapping peaks centred around 2.9 Å. This observation is in good agreement with the studies reporting the distance between the copper atoms decreases by around. 0.1 Å upon dehydration.[69, 70] In the range 325-370 °C, HKUST-1 correlations still dominate. Moreover, increasingly sharp intense peaks assigned to metallic copper can also be clearly observed in the same temperature range. These peaks remain as the only contributor to

the PDF signal at the end of the pyrolysis, as observed by e.g. the nearest neighbour Cu-Cu correlation at 2.6 Å and the next-nearest at 3.6 Å. Correlations from metallic copper extend far in real space (Fig. S20) due to its ordered structure.

Peaks belonging to copper(I) oxide can be spotted at 1.9 Å (nearest Cu-O) and 3.0 Å (nearest Cu-Cu) above 370 °C. However, these correlations and those extending further in real space are difficult to assign due to significant peak overlap between the three copper phases (see calculated patterns in Fig. 7), and the low amount of oxide. Above approx. 400 °C, the peaks assigned to Cu_2O have fully disappeared. Indications of the HKUST-1 framework breakdown above approx. 350 °C are seen by a decreased intensity of the Cu-Cu correlation (at 9.6 Å) between two neighbouring paddlewheels across the organic linker.

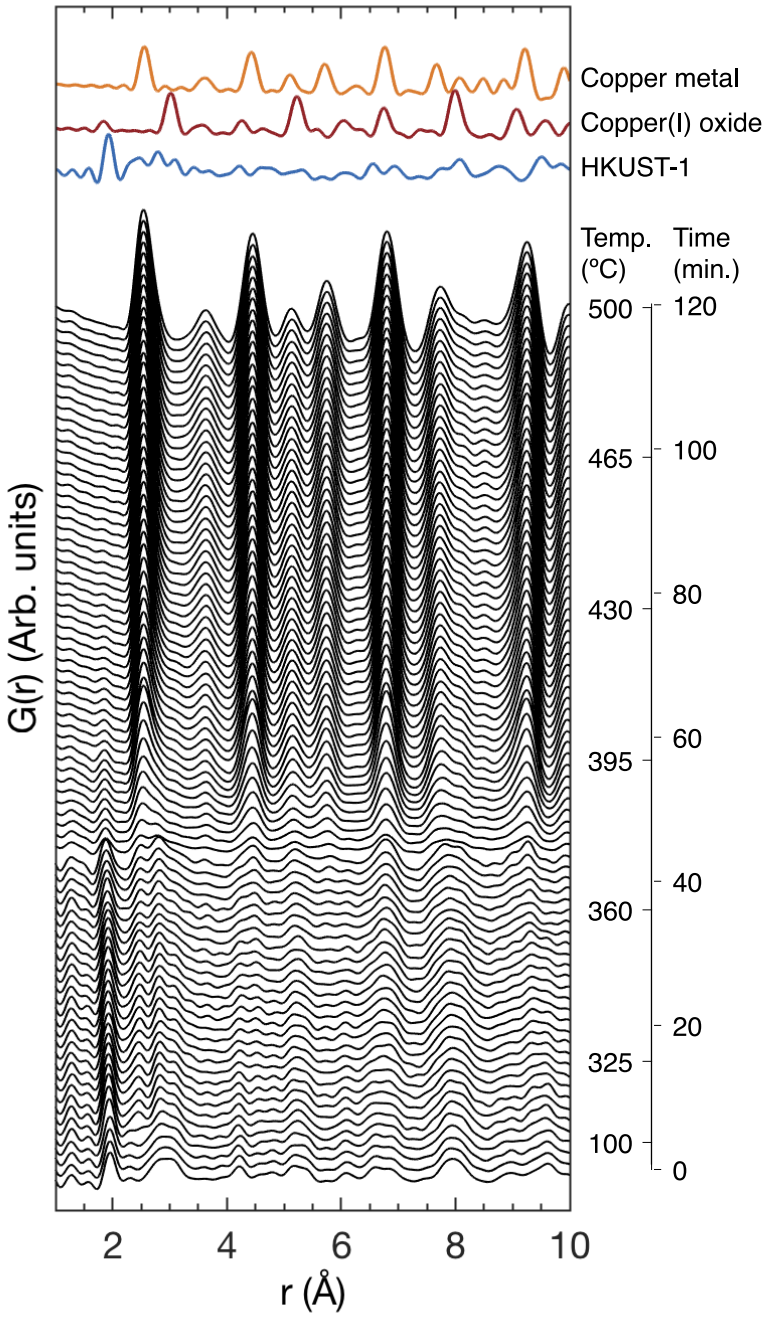

342

343 **Fig. 7.** *In situ* PDF data of HKUST-1 pyrolysis (2 °C/min) with calculated PDFs of metallic copper (yellow),
344 copper(I) oxide (red), and dehydrated HKUST-1 (blue). A combined temperature/time axis is shown in the right
345 of the figure.

346

347 Real-space Rietveld-like multiphase refinements were performed on the *in situ* series (in the
348 range 1-40 Å) to quantify the phase evolution during pyrolysis (Fig. 8). Selected fits are pre-
349 sented in Fig. S21, and all refined parameters are tabulated (Table S4). Below 325 °C the phase

contents are unchanged at 91 wt% HKUST-1 and 9 wt% copper(I) oxide impurity. The first refinement (at 80 °C) uses a hydrated HKUST-1 structural model[30] whereas at higher temperatures a dehydrated model[71] was used due to improvement in the goodness of fit and in agreement with the observed dehydration of HKUST-1. Upon reaching decomposition above 325 °C, copper(I) oxide and metallic copper are formed. The oxide constitutes at its maximum 25.2 wt% of the mixture at 376 °C, after which it is further reduced to the metal, and above 462 °C all Cu_2O has been converted to copper. The quality of the fit improves drastically above around 370 °C due to the formation of highly ordered metallic copper (Table S4). Equivalent short-range refinements (1-15 Å) show the same phase evolution (Fig. S22 and Table S5), however with slightly more oxide present (29.8 wt% at 376 °C) indicating that the oxide phase is less ordered at r>15 Å compared to the metallic copper, hence it is only partly crystalline. This observation fits well with the XANES and PXRD data and shows how the techniques are complementary. The PXRD oxide (111) peak is broad but this appears to only be the most crystalline fraction of the oxide.

3.4 Investigating the effect of heating ramp on the thermal decomposition

Aiming at investigating the influence of the heating rate on the phase evolution behaviour and transition temperature, additional total scattering data were collected for experiments conducted with other heating ramps (5 °C/min and rapid heating reaching the target temperature of 500 °C within 8-10 s, see PDFs in Fig. S23 and S25).

Overall, the same behaviour was observed for the 2 °C/min and 5 °C/min heating experiments (Fig. 8 and S24, and Table S4 and S6) with small differences in decomposition temperature of 300 °C at 5 °C/min vs. 325 °C at 2 °C/min. The maximum oxide amount was determined to be 20.2 wt% at 355 °C at 5 °C/min vs. 25.2 wt% at 376 °C at 2 °C/min, and the temperature at which Cu_2O was no longer present was found to be 450 °C at 5 °C/min vs. 470 °C at 2 °C/min).

These differences are relatively small when considering that these experiments were performed on different beamlines with differences in the heating ramps (see Experimental, Fig. S2 and additional information in the ESI).

Interestingly, there are indications that upon rapid heating (reaching 500 °C within 8-10 s) the oxide phase is either completely bypassed or only exists very briefly (Fig. S25-26 and Table S7). This observation, however, may be explained by the limited time/temperature resolution achieved in this experiment, and the formation mechanism may be similar to that of slower heating ramps.

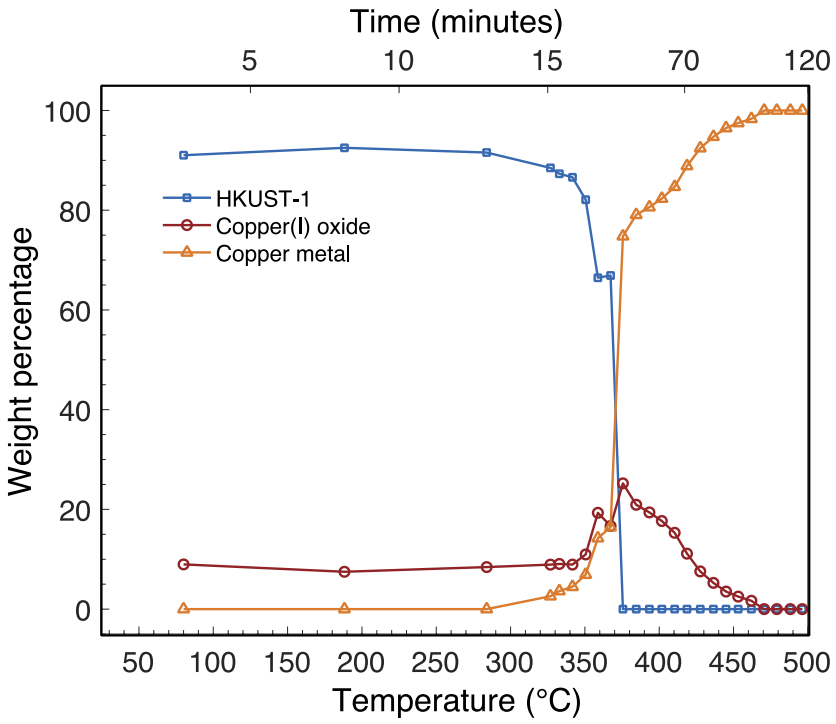

Fig. 8. Phase content evolution of HKUST-1 pyrolysis as obtained from real-space refinement of PDF data (2 °C/min): HKUST-1 (blue), copper(I) oxide (red), and copper metal (yellow).

3.5 Mechanism behind the thermal decomposition of HKUST-1

Across the three techniques, the same decomposition products are observed. Copper(I) oxide and metallic copper are formed upon thermal decomposition of HKUST-1, and at temperatures above 350-470 °C only the metal remains. While it seems plausible that HKUST-1 is reduced

to the oxide which in turn is reduced to the metal, the described results do not rule out that HKUST-1 can also be directly reduced to metal, rather than in a two-step process *via* the oxide. Some differences are seen across the different techniques and by applying different heating ramps with respect to the decomposition temperature and sample composition, but these might partly be a result of using different experimental setups (e.g. furnace setup used for XAS and PXRD versus hot air blower system used for total scattering).

The biggest difference between the techniques is the temperature at which all oxide has been fully reduced to the metal; PXRD and XANES LCA find this to occur at approx. 350 °C, whereas PDF finds values around 470 °C. If we exclude experimental issues due to a potential difference in temperature calibration between the setups, this might be explained by the fact that PDF probes the local to medium range structure, while PXRD probes long range, and XANES LCA assumes that the crystalline standards used as the linear components describe the investigated sample. In other words, any amorphous oxide might first be fully reduced at higher temperatures than 300-350 °C, i.e. the transition interval of crystalline Cu_2O to Cu as observed by PXRD. Therefore, we propose that the difference in transition temperature may most likely be explained by the fact that the non-negligible fraction of the starting material containing Cu(I), is not fully reduced until approx. 470 °C. If the amorphous Cu(I) phase is reduced at higher temperatures than the Cu_2O phase formed by reduction of HKUST-1, this might explain the non-sudden phase transition for PDF, as the Cu(I) reduction takes place over a large temperature interval of more than 100 °C (approx. 350-470 °C) in PDF. This is in contrast to the Cu(I) to Cu(0) transition interval of around 50 °C (approx. 300-350 °C) as observed by XAS and PXRD.

A reported *in situ* PXRD study covering the temperature range from room temperature to 400 °C showed that upon thermal decomposition of the MOF in a sealed ampule, hydrated

HKUST-1 decomposes into another copper(II) coordination polymer [Cu_2(btc)(OH)(H_2O)] before decomposition into the oxide.[72] Furthermore, they found that dehydrated HKUST-1 circumvents this intermediary structure. Since our study occurs in a flow of inert gas, the dehydrated structure is achieved before decomposition and thus this intermediary coordination polymer is not seen.

Several *ex situ* studies of the pyrolysis of HKUST-1 have previously been reported. One study connects the pyrolysis product of various MOFs with the reduction potential of the metal ion, such that Cu^{2+} decomposes into pure metal nanoparticles in agreement with most studies, as it is thermodynamically unfavourable to form oxides.[73] However, several literature studies still report copper(I) and even copper(II) oxides together with the metal upon HKUST-1 pyrolysis.[39, 42, 48, 52] With the knowledge from our work, it can then be stated that although thermodynamically the pure metal will be the final product at sufficiently high temperatures, at temperatures closer to the decomposition point, mixtures of metallic copper and copper(I) oxide will exist. Furthermore, we propose that any observed copper(II) oxide is a result of post-oxidation in air.

3.6 Comparison of three techniques for *in situ* pyrolysis studies

In this work, the three *in situ* techniques used agree on the phase evolution mechanism upon pyrolysis of HKUST-1, meaning that across short (XAS and PDF) and long range order (PXRD), the same phases exist. The use of PXRD, PDF, and XAS together serve as a powerful toolbox for investigations of the structural changes related to MOF-to-MDN transformation. PDF and XAS show how the parent framework breaks down and forms new particles and probe local order from nearest-neighbour bond distances to the sizes of nanoparticles for crystalline and amorphous compounds. PXRD, in contrast, shows the change on a long range scale limited to crystalline materials. It is a powerful technique for structural characterization from which information on e.g. particle size is readily obtainable in addition to quantification of structural

details such as water content in the pores. However, short range sensitive techniques such as PDF and XAS are needed in the case of very small particles, single atom sites, and amorphous phases – all of which are frequently found in the decomposition products of MOFs. In other words, for a compound such as crystalline HKUST-1 transforming into crystalline compounds, *in situ* PXRD alone provides substantial information on the phase composition and particle sizes, according to this study. However, despite the crystalline products formed, PDF and XAS provide information on a significant amorphous phase even in this study. Moreover, PDF and/or XAS are needed if (*i*) a study focuses on the pyrolysis of an amorphous coordination polymer, i.e. a class of compounds currently attracting increased attention,[74, 75] or (*ii*) if it is unknown whether disordered intermediates or products form during pyrolysis of a crystalline MOF. Also, herein, PDF analysis provides in-depth structural details such as the change in Cu-Cu distance in the paddlewheel upon dehydration. Overall, there is a good agreement between PXRD and PDF data as seen from the scale factor evolution of HKUST-1, Cu_2O and Cu (Fig. S27).

With the knowledge obtained in this study, targeted synthesis of materials containing different compositions of HKUST-1/Cu_2O/Cu, hence with different properties, is possible. Such mixtures with a copper(I) oxide content of up to approx. 25 wt% can be obtained by terminating the pyrolysis at the temperature corresponding to a given mixture. The *in situ* studies give a clear insight into the mechanism of the phase transition and elucidate the phase compositions achievable by pyrolysis of HKUST-1 under inert conditions up to 500 °C. However, in order to prepare upscaled samples with the desired composition, adaption to a laboratory setup is needed, as the sample composition changes fast with time and temperature and is dependent on the specific pyrolysis setup. Yet, the *in situ* studies reduces the parameter space to be explored in the development of protocols for preparing MDNs, as it is known what phase compositions are achievable within an approximate temperature range.

In this study, we did not focus on the carbon phase formed during pyrolysis as the low scattering power of carbon compared to copper results in a significantly reduced sensitivity of the X-ray scattering techniques. According to CHNS analysis, the material has a composition of $CuC_{2.49}H_{0.81}$ (not analysed for oxygen) after pyrolysis in a tube furnace at 2 °C/min. For comparison as-synthesized dehydrated HKUST-1 has a composition of $CuC_6H_2(O_4)$, proposing approximately half of the carbon content after pyrolysis (see also Table S1). For additional studies of the carbon matrix, we propose *ex situ* techniques such as X-ray photoelectron spectroscopy (XPS) and electron microscopy techniques which can be used to obtain information on the carbon phase. Alternatively, differential PDF or neutron scattering could be used to facilitate this fascinating but challenging issue, or chemical post-treatment of the sample could be performed to yield a copper-free carbon.

4 Conclusion

In conclusion, the structural changes during thermal decomposition of the archetypical metal-organic framework HKUST-1 has been investigated *in situ* using three complementary X-ray based techniques: absorption spectroscopy, powder diffraction, and total scattering/PDF analysis. Detailed information on the phase evolution and composition, particle sizes of crystalline phases, and oxidation state is readily extracted from the experimental data in addition to details on e.g. changes in the local coordination environment.

The framework decomposes between 300 and 325 °C, and the final pyrolysis product is highly ordered, metallic copper nanoparticles (65-80 nm crystallites). It is found that the pathway from MOF to metal goes through copper(I) oxide (approx. 13 nm) with some indications that at very fast heating rates, the oxide might be circumvented.

We believe this work serves as a benchmark study of how the combination of PXRD probing long-range crystalline order with PDF and XAS for local structural investigations function very

well for investigating the formation of MOF-derived materials. The methodology is generally applicable and can easily be extended to other crystalline or amorphous coordination polymers.

Acknowledgements

The work was supported by the Carlsberg Foundation (CF17-0937, CF18-0840 and CF19-0585), Independent Research Fund Denmark (8021-00349B), Aarhus University Research Foundation (AUFF-E-2015-FLS-7-24), The Danish National Research Foundation (Carbon Di-oxide Activation Center, DNRF 118), and DanScatt. Affiliation with the Center for Integrated Materials Research (iMAT) at Aarhus University and the Sino-Danish Center for Education and Research is gratefully acknowledged.

Cecilie Nielsen is kindly thanked for acquisition of CHNS data. We acknowledge DESY (Ham-burg, Germany), a member of the Helmholtz Association HGF, for the provision of experi-mental facilities. Parts of this research were carried out at PETRA III and we would like to thank Alexander Schökel and Ann-Christin Dippel for assistance in using P02.1 and P21.1. Likewise, we acknowledge the Diamond Light Source for beamtime on B18 (proposal number SP22410).

Conflicts of interest

There are no conflicts of interest to declare.

References

1. O. M. Yaghi, D. A. Richardson, G. Li, C. E. Davis and T. L. Groy, *MRS Proceedings*, 1994, **371**, 15-19.
2. Cambridge Structural Database (CSD) MOF subset.
3. H.-C. J. Zhou and S. Kitagawa, *Chemical Society Reviews*, 2014, **43**, 5415-5418.
4. J. Gascon, A. Corma, F. Kapteijn and F. X. Llabrés i Xamena, *ACS Catalysis*, 2014, **4**, 361-378.

5. H. Li, K. Wang, Y. Sun, C. T. Lollar, J. Li and H.-C. Zhou, *Materials Today*, 2018, **21**, 108-121.
6. L. E. Kreno, K. Leong, O. K. Farha, M. Allendorf, R. P. Van Duyne and J. T. Hupp, *Chemical Reviews*, 2012, **112**, 1105-1125.
7. M. Ding, X. Cai and H.-L. Jiang, *Chemical Science*, 2019, **10**, 10209-10230.
8. A. J. Howarth, Y. Liu, P. Li, Z. Li, T. C. Wang, J. T. Hupp and O. K. Farha, *Nature Reviews Materials*, 2016, **1**, 15018.
9. C. Healy, K. M. Patil, B. H. Wilson, L. Hermanspahn, N. C. Harvey-Reid, B. I. Howard, C. Kleinjan, J. Kolien, F. Payet, S. G. Telfer, P. E. Kruger and T. D. Bennett, *Coordination Chemistry Reviews*, 2020, **419**, 213388.
10. G. Mouchaham, S. Wang and C. Serre, Wiley-VCH Verlag GmbH & Co. KGaA, 2018, pp. 1-28.
11. S. Yuan, L. Feng, K. Wang, J. Pang, M. Bosch, C. Lollar, Y. Sun, J. Qin, X. Yang, P. Zhang, Q. Wang, L. Zou, Y. Zhang, L. Zhang, Y. Fang, J. Li and H.-C. Zhou, *Advanced Materials*, 2018, **30**, 1704303.
12. S. Frank, E. Svensson Grape, E. D. Bøjesen, R. Larsen, P. Lamagni, J. Catalano, A. K. Inge and N. Lock, *Journal of Materials Chemistry A*, 2021, **9**, 26298-26310.
13. L. Oar-Arteta, T. Wezendonk, X. Sun, F. Kapteijn and J. Gascon, *Materials Chemistry Frontiers*, 2017, **1**, 1709-1745.
14. K. J. Lee, J. H. Lee, S. Jeoung and H. R. Moon, *Accounts of Chemical Research*, 2017, **50**, 2684-2692.
15. W. Xia, A. Mahmood, R. Zou and Q. Xu, *Energy & Environmental Science*, 2015, **8**, 1837-1866.
16. Y. Song, X. Li, L. Sun and L. Wang, *RSC Advances*, 2015, **5**, 7267-7279.
17. X. F. Lu, Y. Fang, D. Luan and X. W. D. Lou, *Nano Letters*, 2021, **21**, 1555-1565.
18. S. J. Yang, S. Nam, T. Kim, J. H. Im, H. Jung, J. H. Kang, S. Wi, B. Park and C. R. Park, *Journal of the American Chemical Society*, 2013, **135**, 7394-7397.
19. A. Mohammadi Zardkhoshoui and S. S. Hosseiny Davarani, *Nanoscale*, 2020, **12**, 12476-12489.
20. F. Zheng, S. Xu, Z. Yin, Y. Zhang and L. Lu, *RSC Advances*, 2016, **6**, 93532-93538.
21. S. Wang, J. Teng, Y. Xie, Z.-W. Wei, Y. Fan, J.-J. Jiang, H.-P. Wang, H. Liu, D. Wang and C.-Y. Su, *Journal of Materials Chemistry A*, 2019, **7**, 4036-4046.
22. D. Huang, G. Wang, M. Cheng, G. Zhang, S. Chen, Y. Liu, Z. Li, W. Xue, L. Lei and R. Xiao, *Chemical Engineering Journal*, 2021, **421**, 127817.
23. M. Z. Hussain, M. Bahri, W. R. Heinz, Q. Jia, O. Ersen, T. Kratky, R. A. Fischer, Y. Zhu and Y. Xia, *Microporous and Mesoporous Materials*, 2021, **316**, 110957.
24. G. Li, H. Kobayashi, K. Kusada, J. M. Taylor, Y. Kubota, K. Kato, M. Takata, T. Yamamoto, S. Matsumura and H. Kitagawa, *Chemical Communications*, 2014, **50**, 13750-13753.
25. C. Wu, D. Xie, Y. Mei, Z. Xiu, K. M. Poduska, D. Li, B. Xu and D. Sun, *Physical Chemistry Chemical Physics*, 2019, **21**, 17571-17577.
26. J. Li, L. Jiao, E. Wegener, L. L. Richard, E. Liu, A. Zitolo, M. T. Sougrati, S. Mukerjee, Z. Zhao, Y. Huang, F. Yang, S. Zhong, H. Xu, A. J. Kropf, F. Jaouen, D. J. Myers and Q. Jia, *Journal of the American Chemical Society*, 2020, **142**, 1417-1423.
27. T. A. Wezendonk, V. P. Santos, M. A. Nasalevich, Q. S. E. Warringa, A. I. Dugulan, A. Chojecki, A. C. J. Koeken, M. Ruitenbeek, G. Meima, H.-U. Islam, G. Sankar, M. Makkee, F. Kapteijn and J. Gascon, *ACS Catalysis*, 2016, **6**, 3236-3247.
28. A. Li, Y. Tong, H. Song and X. Chen, *The Journal of Physical Chemistry C*, 2018, **122**, 17278-17286.

29. N. Prinz, L. Schwensow, S. Wendholt, A. Jentys, M. Bauer, W. Kleist and M. Zobel, *Nanoscale*, 2020, **12**, 15800-15813.
30. S. Y. Chui Stephen, M. F. Lo Samuel, P. H. Charmant Jonathan, A. G. Orpen and D. Williams Ian, *Science*, 1999, **283**, 1148-1150.
31. K. Schlichte, T. Kratzke and S. Kaskel, *Microporous and Mesoporous Materials*, 2004, **73**, 81-88.
32. C. Wei, X. Li, F. Xu, H. Tan, Z. Li, L. Sun and Y. Song, *Analytical Methods*, 2014, **6**, 1550-1557.
33. Y. Wang, Y. Lü, W. Zhan, Z. Xie, Q. Kuang and L. Zheng, *Journal of Materials Chemistry A*, 2015, **3**, 12796-12803.
34. Y. Xie, Y. Song, Y. Zhang, L. Xu, L. Miao, C. Peng, L. Wang, *Journal of Alloys and Compounds*, 2018, **757**, 105-111.
35. L. Hu, Y. Huang, F. Zhang and Q. Chen, *Nanoscale*, 2013, **5**, 4186-4190.
36. L. J. Wang, X. Wang, Z. Meng, H. Hou and B. Chen, *Journal of Materials Science*, 2017, **52**, 7140-7148.
37. R. Wu, X. Qian, F. Yu, H. Liu, K. Zhou, J. Wei and Y. Huang, *Journal of Materials Chemistry A*, 2013, **1**, 11126-11129.
38. A. Y. Kim, M. K. Kim, K. Cho, J.-Y. Woo, Y. Lee, S.-H. Han, D. Byun, W. Choi and J. K. Lee, *ACS Applied Materials & Interfaces*, 2016, **8**, 19514-19523.
39. R. Zhang, L. Hu, S. Bao, R. Li, L. Gao, R. Li and Q. Chen, *Journal of Materials Chemistry A*, 2016, **4**, 8412-8420.
40. S. Zhang, H. Liu, C. Sun, P. Liu, L. Li, Z. Yang, X. Feng, F. Huo and X. Lu, *Journal of Materials Chemistry A*, 2015, **3**, 5294-5298.
41. Y. Yang, H. Dong, Y. Wang, Y. Wang, N. Liu, D. Wang and X. Zhang, *Inorganic Chemistry Communications*, 2017, **86**, 74-77.
42. K. Zhao, Y. Liu, X. Quan, S. Chen and H. Yu, *ACS Applied Materials & Interfaces*, 2017, **9**, 5302-5311.
43. K. Yao, Y. Xia, J. Li, N. Wang, J. Han, C. Gao, M. Han, G. Shen, Y. Liu, A. Seifitokaldani, X. Sun and H. Liang, *Journal of Materials Chemistry A*, 2020, **8**, 11117-11123.
44. A. V. Rayer, E. Reid, A. Kataria, I. Luz, S. J. Thompson, M. Lail, J. Zhou and M. Soukri, *Journal of CO2 Utilization*, 2020, **39**, 101159.
45. D. Li, T. Liu, Z. Yan, L. Zhen, J. Liu, J. Wu and Y. Feng, *ACS Applied Materials & Interfaces*, 2020, **12**, 7030-7037.
46. H. Kaimeng, C. Siyuan, X. Changjiu, L. Chenhao, Z. Bin, G. Hongyi, P. Xinxin, L. Min, L. Yibin, W. Ge and S. Xingtian, *RSC Advances*, 2020, **10**, 36111-36118.
47. J. Li, W. Liu, Y. Ding, L. Liu, F. Li and Q. Li, *Korean Journal of Chemical Engineering*, 2019, **36**, 851-859.
48. Q. Zhang, J. Zuo, F. Peng, S. Chen, Q.-y. Wang and Z.-l. Liu, *ChemistrySelect*, 2019, 4, 13517-13524.
49. X. Liu, D. Xu and L. Zhang, *ACS Sustainable Chemistry & Engineering*, 2017, **5**, 7800-7811.
50. K. Yang, Y. Yan, H. Wang, Z. Sun, W. Chen, H. Kang, Y. Han, W. Zahng, X. Sun and Z. Li, *Nanoscale*, 2018, **10**, 17647-17655.
51. X. Han, X. He, L. Sun, X. Han, W. Zhan, J. Xu, X. Wang and J. Chen, *ACS Catalysis*, 2018, **8**, 3348-3356.
52. Y. Weng, S. Guan, L. Wang, H. Lu, X. Meng, G. I. N. Waterhouse and S. Zhou, *Small*, 2020, **16**, 1905184.

53. A. J. Dent, G. Cibin, S. Ramos, A. D. Smith, S. M. Scott, L. Varandas, M. R. Pearson, N. A. Krumpa, C. P. Jones and P. E. Robbins, *Journal of Physics: Conference Series*, 2009, **190**, 012039.
54. K. Klementiev and R. Chernikov, *Journal of Physics: Conference Series*, 2016, **712**, 012008.
55. B. Ravel and M. Newville, *Journal of Synchrotron Radiation*, 2005, **12**, 537-541.
56. TOPAS V4. Bruker AXS 2008, Karlsruhe, Germany.
57. R. W. Cheary and A. Coelho, *Journal of Applied Crystallography*, 1992, **25**, 109-121.
58. A. Katerinopoulou, T. Balic-Zunic and L. F. Lundegaard, *Journal of Applied Crystallography*, 2012, **45**, 22-27.
59. C. F. Macrae, I. J. Bruno, J. A. Chisholm, P. R. Edgington, P. McCabe, E. Pidcock, L. Rodriguez-Monge, R. Taylor, J. Van De Streek and P. A. Wood, *Journal of Applied Crystallography*, 2008, **41**, 466-470.
60. A.-C. Dippel, H.-P. Liermann, J. T. Delitz, P. Walter, H. Schulte-Schrepping, O. H. Seeck and H. Franz, *Journal of Synchrotron Radiation*, 2015, **22**, 675-687.
61. J. Becker, M. Bremholm, C. Tyrsted, B. Pauw, K. M. Ø. Jensen, J. Eltzholt, M. Christensen and B. B. Iversen, *Journal of Applied Crystallography*, 2010, **43**, 729-736.
62. C. Prescher and V. B. Prakapenka, *High Pressure Research*, 2015, **35**, 223-230.
63. P. Juhas, T. Davis, C. L. Farrow and S. J. L. Billinge, *Journal of Applied Crystallography*, 2013, **46**, 560-566.
64. X. Yang, P. Juhas, C. L. Farrow and S. J. L. Billinge, *arXiv*, 2015, **arXiv:1402.3163 [cond-mat.mtrl-sci]**.
65. C. L. Farrow, P. Juhas, J. W. Liu, D. Bryndin, E. S. Božin, J. Bloch, P. Th and S. J. L. Billinge, *Journal of Physics: Condensed Matter*, 2007, **19**, 335219.
66. A. Kuzmin and J. Chaboy, *IUCrJ*, 2014, **1**, 571-589.
67. J. Timoshenko, A. Halder, B. Yang, S. Seifert, M. Pellin, S. Vajda and A. Frenkel, *The Journal of Physical Chemistry C*, 2018, **122**, 21686-21693.
68. Y. Liu, N. Marcella, J. Timoshenko, A. Halder, B. Yang, L. Kolipaka, M. J. Pellin, S. Seifert, S. Vajda, P. Liu and A. I. Frenkel, *The Journal of Chemical Physics*, 2019, **151**, 164201.
69. C. Prestipino, L. Regli, J. G. Vitillo, F. Bonino, A. Damin, C. Lamberti, A. Zecchina, P. L. Solari, K. O. Kongshaug and S. Bordiga, *Chemistry of Materials*, 2006, **18**, 1337-1346.
70. T. Watanabe and D. S. Sholl, *The Journal of Chemical Physics*, 2010, **133**, 094509.
71. V. K. Peterson, P. D. Southon, G. J. Halder, D. J. Price, J. J. Bevitt and C. J. Kepert, *Chemistry of Materials*, 2014, **26**, 4712-4723.
72. M. Schlesinger, S. Schulze, M. Hietschold and M. Mehring, *Microporous and Mesoporous Materials*, 2010, **132**, 121-127.
73. R. Das, P. Pachfule, R. Banerjee and P. Poddar, *Nanoscale*, 2012, **4**, 591-599.
74. T. D. Bennett and A. K. Cheetham, *Accounts of Chemical Research*, 2014, **47**, 1555-1562.
75. T. D. Bennett and S. Horike, *Nature Reviews Materials*, 2018, **3**, 431-440.